Electronic Supplementary Information

Robust FeOOH/$BiVO_4$/Cu(In,Ga)Se_2 Tandem Structure for Solar-Powered Biocatalytic CO_2 Reduction

*Jinhyun Kim†, Yang Woo Lee†, Eun-Gyu Choi, Passarut Boonmongkolras, Byoung Wook Jeon, Hojin Lee, Seung Tae Kim, Su Keun Kuk, Yong Hwan Kim, Byungha Shin, and Chan Beum Park**

Department of Materials Science and Engineering, Korea Advanced Institute of Science and Technology (KAIST), 335 Science Road, Daejeon 305-701, Republic of Korea; School of Energy and Chemical Engineering, Ulsan National Institute of Science and Technology (UNIST), 50 UNIST-gil, Ulsan, 44919, Republic of Korea

†J. Kim and Y. W. Lee contributed equally to this work.
*E-mail: parkcb@kaist.ac.kr

Experimental procedures

Chemicals

Potassium hydride, ethanol, bismuth(III) nitrate pentahydrate, potassium iodide, ethanol, nitric acid, *p*-benzoquinone, vanadyl acetylacetonate, dimethyl sulfoxide (DMSO), indium tin oxide nanopowder, acetic acid, β-NAD^+ hydrate (NAD^+), and sodium formate were purchased from Sigma-Aldrich (St. Louis, MO, USA). These chemicals were used without further purification. We used type 1 ultrapure water (18 MΩ cm) from a Direct-Q® 5 UV ultrapure water purification system (Millipore Corp., USA) for preparing a buffer solution. $[Cp^*Rh(bpy)H_2O]^{2+}$ and *Ts*FDH were produced according to the literature[1, 2].

Fabrication of photovoltaics

We synthesized a CIGS photovoltaic in a Mo/CIGS/CdS/i-ZnO/ZnO:Al/Al-grid architecture according to the literature procedure[3] with a slight modification. We deposited a CIGS absorber layer on a Mo-coated soda-lime glass via co-evaporation of Cu, In, Ga, and Se from elemental effusion cells in a vacuum evaporator at a base pressure of 2.7×10^{-4} Pa. The

average [Cu]/([Ga]+[In]), [Ga]/([Ga]+[In]), and thickness of the CIGS layer were in the range of 0.80-0.90, 0.30-0.35, and 1.8-2.0 μm, respectively. After the deposition, the CIGS film was immersed in a 0.15 M KCN solution for 1-min etching, rinsed with deionized water, and annealed in Se atmosphere at 473 K. To deposit a CdS buffer layer (40-50 nm) on the as-synthesized CIGS film, we performed the chemical bath deposition process for 6 min using $CdSO_4$ as a Cd ion source, thiourea as a sulfur source, and NH_3 as a complexing agent. Then, we used radio frequency magnetron sputtering to deposit a bilayer, which consisted of i-ZnO layer (50 nm) and an Al-doped ZnO layer (ZnO:Al, 350 nm). Lastly, we deposited Al electrode via thermal evaporation of Al through an aperture mask. As a control group, a perovskite solar cell (PSC) with a light absorber containing triple cations (*i.e.*, Cs^+, methylammonium, and formamidinium) was fabricated following a literature procedure[4] reported previously. The structure of the PSC was FTO/SnO_2/perovskite/2,2′,7,7′-tetrakis(N,N′-di-*p*-methoxyphenylamine)-9,9′-spirobifluorene/Au.

Characterization of solar cells

We used a K3000 Solar Simulator (McScience Inc., Korea) to measure *J-V* characteristics under one-sun illumination (AM 1.5G, 100 mW cm^{-2}), which was calibrated with a silicon reference cell. The power conversion efficiency (PCE) was calculated using eqn (S1)

$$\text{PCE}\ (\%) = \frac{J_{\text{sc}} \times V_{\text{oc}} \times \text{FF}}{P} \qquad \text{(S1)}$$

where *J*sc is the short-circuit current density (mA cm^{-2}), V_{oc} is the open-circuit voltage (V), FF is the fill factor, and *P* is the incident illumination power density (mW cm^{-2}). An external quantum efficiency was obtained using a QEX7 solar cell spectral response/QE/IPCE measurement system (PV Measurement Inc., USA). The light absorption of a solar cell was

investigated using a SolidSpec-3700 UV-VIS-NIR Spectrophotometer (Shimadzu Corp., Japan).

Fabrication of photoanode

A commercial FTO glass (TEC-7, Pilkington) was thoroughly rinsed with 1.0 M KOH aqueous solution, deionized water, and ethanol. The electrodeposition of a BiOI film on the FTO were performed using potentiostat/galvanostat (WMPG 1000, WonATech Co., Korea); the FTO substrate was immersed in a BiOI precursor solution and applied an external bias of -0.1 V (vs. Ag/AgCl) to the substrate. The three-electrode configuration consisted of a working electrode, a reference electrode (Ag/AgCl, 3 M NaCl), and the counter electrode (stainless steel). The precursor solution was prepared by dissolving $Bi(NO_3)_3 \cdot 5H_2O$ (40 mM), HNO_3 (3 μl ml^{-1}), and KI (40 M) in deionized water (100 ml) and adding a 40-ml ethanolic solution containing *p*-benzoquinone (115.6 mM). To transform BiOI into $BiVO_4$, we dropped a V-containing solution on the BiOI electrode and heated it in a Lindberg/Blue M muffle furnace (Fisher Scientific Corp., USA) at 723 K for 2 h with a ramping rate of 1 K min^{-1}. The precursor solution was prepared by dissolving $VO(acac)_2$ (51.2 mg) in anhydrous DMSO (1 ml). After the reaction, we eliminated brownish V_2O_5 crusts on the surface of a $BiVO_4$ by soaking it in a NaOH solution (1 M) with gentle stirring. For photo-assisted electrodeposition of FeOOH cocatalyst on a $BiVO_4$ electrode, we immersed the $BiVO_4$ in a $FeSO_4$ aqueous solution (100 mM) with vigorous stirring and applied it at 0.3 V (vs. Ag/AgCl) under irradiation with white LED light (2 mW cm^{-2}). We prepared a FeOOH electrode as a control group; a FTO substrate was immersed in a $FeSO_4$ solution (100 mM) and applied at 1.42 V (vs. Ag/AgCl) for 10 min to pass a total charge of ca. 43 mC cm^{-2}. We used a SolidSpec-3700 UV-VIS-NIR Spectrophotometer (Shimadzu Corp., Japan) to obtain the absorption spectrum of the FeOOH/$BiVO_4$ electrode.

Fabrication of photoanode/photovoltaic tandem cells

A FeOOH/$BiVO_4$/CIGS tandem cell was prepared through wiring a FeOOH/$BiVO_4$ photoanode to a CIGS solar cell. The CIGS solar cell was covered with transparent, waterproof epoxy. Then, we covered the Al grid with a Ag paste and attached a Cu tape on the side for further wiring to a cathode. On the other hand, we stuck a Cu tape on the Mo side of the CIGS, which was connected to the FTO side of the FeOOH/$BiVO_4$. Finally, we used an opaque epoxy resin to cover the other sides of FeOOH/$BiVO_4$/CIGS device (except the Cu tape on Ag paste and the front side of FeOOH/$BiVO_4$) for blocking out an incident light and avoiding direct contact between an electrolyte solution and a conductive part of the tandem cell. When we assembled a FeOOH/$BiVO_4$/Perovskite tandem device, we stuck a Cu tape on the Au contact of the PSC (hole collector), which was wired to the FTO side of the photoanode. Another Cu tape was attached on the FTO side of the PSC (electron collector) for further wiring to a cathode. The other sides of the PSC was covered with an epoxy resin to protect the solar cell from environment.

Preparation of mesoITO electrode

We modified the method to synthesize a *meso*ITO electrode according to the literature.[5] We prepared a ITO suspension—40 mg of ITO nanoparticles (< 50 nm in diameter) in a 193 μl of acetic acid/ethanol (300:748 v/v) mixture—ultrasonicated it at least 60 min, and homogenized it for 30 min. Then, the ITO suspension (20 μl) was drop-cast onto a FTO substrate (geometrical surface area: 1 cm^2). The electrode was annealed at 673 K for 1 h with a rate of 4 K min^{-1}. We covered an epoxy resin with the other area that was not covered by ITO nanoparticles. As a control group, a planar ITO glass was purchased from Taewon Scientific Corp. (Korea).

(Photo)electrochemical measurements

The (photo)electrochemistry experiments were controlled using a potentiostat/galvanostat (WMPG 1000, WonATech Co., Korea). In a three-electrode configuration, the working electrode, the reference electrode (Ag/AgCl, 3 M NaCl), and the counter electrode (stainless steel) were located in the same compartment. The electrolyte solution consisted of a sodium phosphate buffer (100 mM, pH 7.0). When we conducted controlled potential photoelectrolysis, the light source was a xenon lamp ($\lambda > 400$ nm, P: 100 mW cm^{-2}). All potentials have been quoted vs. RHE according to the following equation (eqn (S2))

$$E_{RHE}\ (V) = E_{Ag/AgCl}\ (V) + 0.209 + (0.059 \times pH) \qquad (S2)$$

Note that platinum is not recommended as a counter electrode during the investigation of a cathodic behavior of a working electrode[6]; as the potential of the Pt becomes positive, the metal undergoes the oxidation and dissolution according to its Pourbaix diagram[7]. Furthermore, the dissolved Pt ions can be deposited on the surface of the working electrode, which influences the electrochemical behavior of the working electrode.[6]

Biocatalytic photoelectrochemical reactions

Cofactor regeneration reaction and water oxidation reaction were fulfilled in two separate reactors connected by a salt bridge. We immersed a FeOOH/$BiVO_4$/CIGS tandem cell in a phosphate buffer (100 mM, pH 7.0) and a *meso*ITO cathode in a phosphate buffer (100 mM, pH 7.0, 2.5 ml) containing 0.5 mM **M** and 1 mM NAD^+; the cathode was connected (through a potentiostat) to the tandem cell in two-electrode configuration. The geometrical surface areas of CIGS, FeOOH/$BiVO_4$, and *meso*ITO were 0.45, 4, and 1 cm^2, respectively. When a CIGS solar cell was replaced with a PSC (geometrical surface area: 0.45 cm^2), we placed the PSC outside a reaction chamber to avoid its direct contact with an aqueous solution. The

photoanode was immersed in the solution at a distance of ca. 3 cm from the PSC. The *meso*ITO cathode was also connected to the tandem cell through a potentiostat. These tandem absorbers were irradiated by a xenon lamp (Newport Co., USA; $\lambda > 400$ nm; *P*: 100 mW cm^{-2}), not the *meso*ITO cathode. We monitored the NADH concentration using a V-650 UV-Vis absorption spectrophotometer (JASCO Inc., Japan); the absorption peak position and the molar extinction coefficient of NADH were 340 nm and 6220 M^{-1} cm^{-1}, respectively.[8] For biocatalytic conversion of CO_2 to formate, we prepared a phosphate buffer (100 mM, pH 7.0, 2.5 ml) containing 0.5 mM **M**, 0.5 mM NAD^+, 10 U ml^{-1} *Ts*FDH, and CO_2; the phosphate buffer was purged with CO_2 gas (99.999%) before and during the redox reaction. We quantified formate using a LC-20A prominence (Shimadzu Corp., Japan). The machine was equipped with a refractive index detector and an Aminex HPX-87H ion exclusion column (Bio-Rad Laboratories Inc., USA). The TOF_{NAD+} and TTN_{NAD+} were calculated according to the following equations (eqn (S3) and (S4))

$$\mathrm{TOF_{NAD^+}}\ (\mathrm{h^{-1}}) = \frac{\text{Concentration of product at the given time}}{\text{Initial concentration of } \mathrm{NAD^+} \times \text{Time}} \tag{S3}$$

$$\mathrm{TTN_{NAD^+}} = \frac{\text{Maximum concentration of product}}{\text{Initial concentration of } \mathrm{NAD^+}} \tag{S4}$$

The solar-to-formate (STF) energy conversion efficiency was estimated according to eqn (S5)

$$\text{STF efficiency}\ (\%) = \frac{r\ (\mathrm{mmol\ s^{-1}}) \times \Delta G^{\circ}\ (\mathrm{J\ mol^{-1}})}{P\ (\mathrm{mW\ cm^{-2}}) \times \text{Area}\ (\mathrm{cm^2})} \times 100 \tag{S5}$$

where *r* is the rate of formate production, *P* is the power density of incident light, and ΔG° is the Gibbs free energy for reduction of gaseous CO_2 to liquid formic acid (270140 J mol^{-1}) based on the chemical reaction: CO_2 (g) + H_2O (l) → HCOOH (l) + 0.5 O_2 (g). The *Ts*FDH's k_{red}/K_M for CO_2 reduction (eqn (S6)) is 3.2-fold lower than that for formate oxidation (eqn (S7)).[2]

$$Ts\text{FDH} + CO_2 + \text{NADH} \rightarrow Ts\text{FDH} + HCOO^- + NAD^+ \tag{S6}$$

$$TsFDH + HCOO^- + NAD^+ \rightarrow TsFDH + CO_2 + NADH \quad \text{(S7)}$$

The k_{red}/K_M for eqn (S6) was estimated using $NaHCO_3$ (CO_2 supplier) and NADH without $HCOO^-$ and NAD^+.[2] In the same manner, that for eqn (S7) was calculated using $HCOO^-$ and NAD^+ in the absence of CO_2 and NADH. Although the k_{red}/K_M for CO_2 reduction is lower than that for formate oxidation, these kinetic parameters cannot solely determine whether CO_2 reduction is faster than formate oxidation because the concentrations of substrates also affect the enzyme kinetics. According to the Michaelis-Menten kinetics, the rate of CO_2 reduction is higher than that of formate oxidation if NADH concentration is much higher than NAD^+ concentration. Thus, NADH-regenerating systems[9-11]—including our tandem cell—promoted *Ts*FDH-driven conversion of CO_2 to formate by keeping NADH/NAD^+ ratio higher.

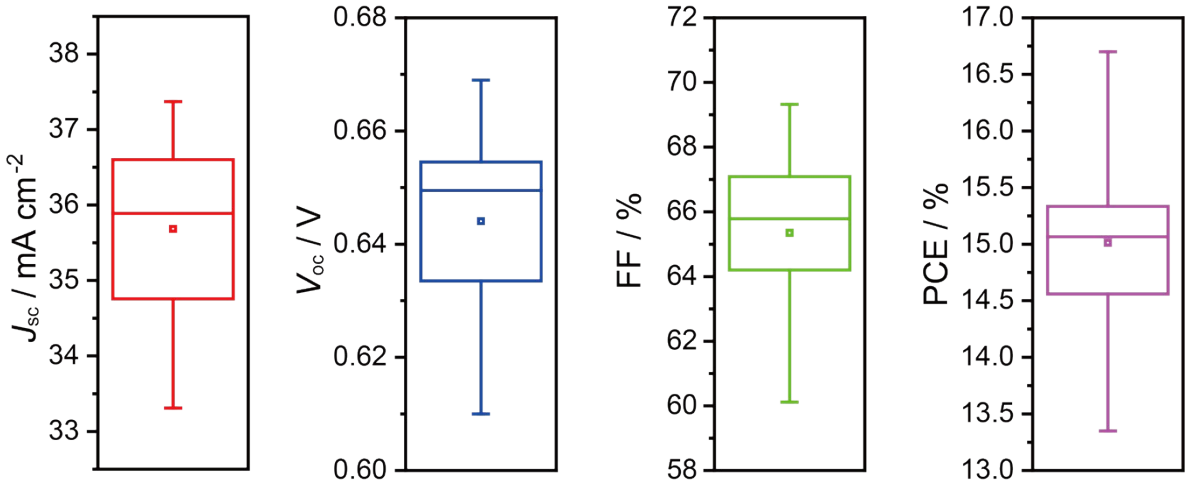

Fig. S1 Box-and-whisker plots of photovoltaic parameters (*e.g.*, J_{sc}, V_{oc}, FF, and PCE) for twenty 0.45-cm^2 CIGS solar cells.

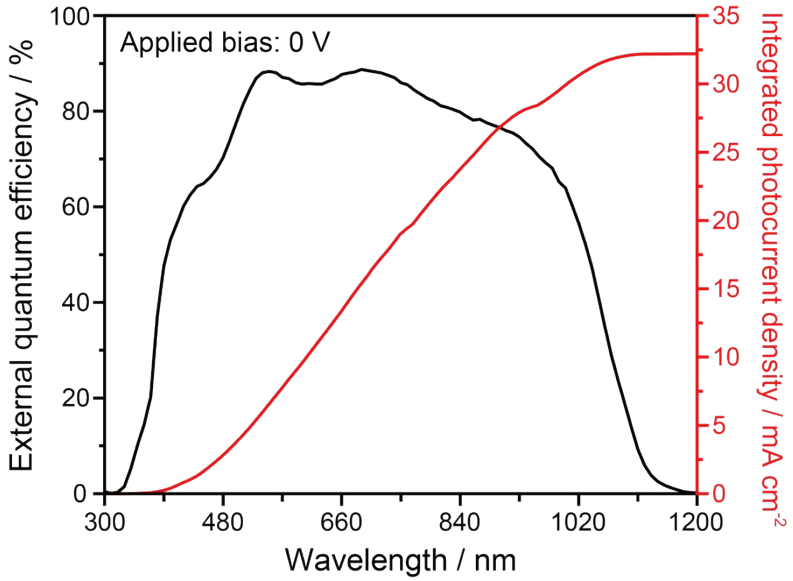

Fig. S2 External quantum efficiency and integrated photocurrent density of CIGS photovoltaic. Applied bias: 0 V.

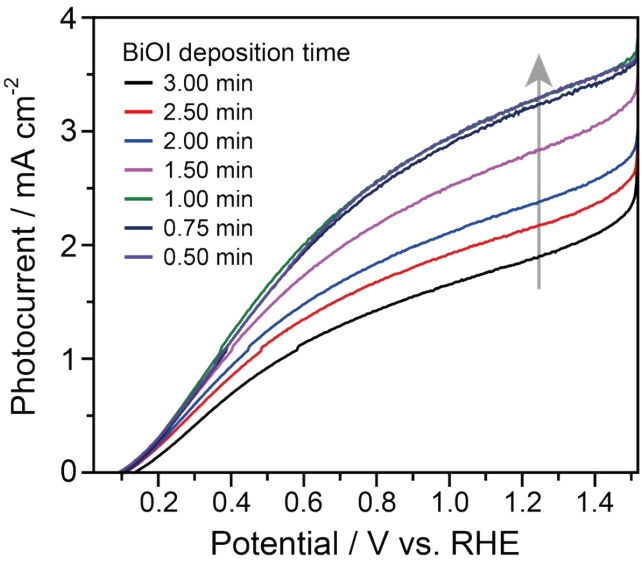

Fig. S3 Effect of BiOI deposition time on the photocurrent of $BiVO_4$ for 500 mM Na_2SO_3 oxidation under front illumination. We optimized the photoanodic current by changing the thickness of BiOI film. As we increased the deposition time of the BiOI, the photocurrent of the $BiVO_4$ decreased (**Fig. S3**) and the thickness of the $BiVO_4$ increased (**Fig. S4(a) and S4(b)**). However, the $BiVO_4$'s nanostructural morphology and crystallinity remained unchanged (**Fig. S4(c), S4(d), and S5**). These results indicate that a small thickness of the $BiVO_4$ photoanode is beneficial for increasing its photoanodic current (under front illumination) because of a shorter migratory route of photoexcited electrons from the $BiVO_4$ to FTO.

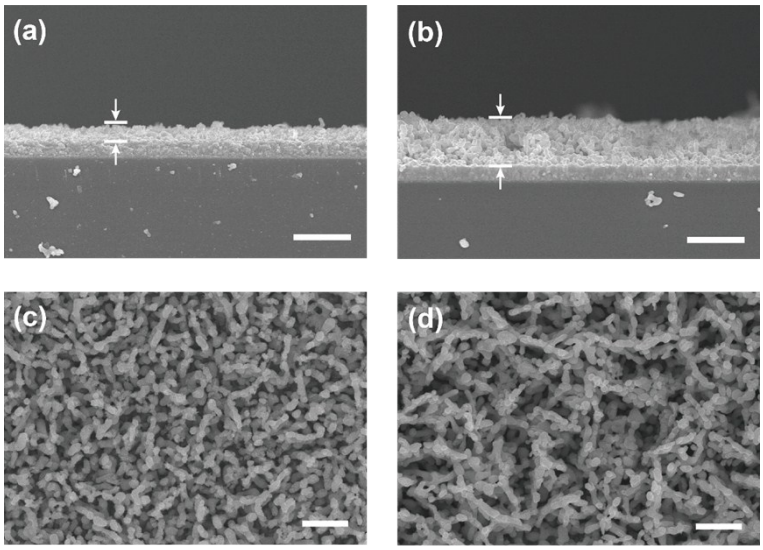

Fig. S4 Plan-view and cross-sectional scanning electron microscopic (SEM) images of $BiVO_4$ electrode. Deposition time of BiOI of (**a**) and (**c**): 1 min. Deposition time of BiOI of (**b**) and (**d**): 3 min. Scale bars of (**a**), (**b**), (**c**) and, (**d**): 2000, 2000, 800, and 800 nm, respectively.

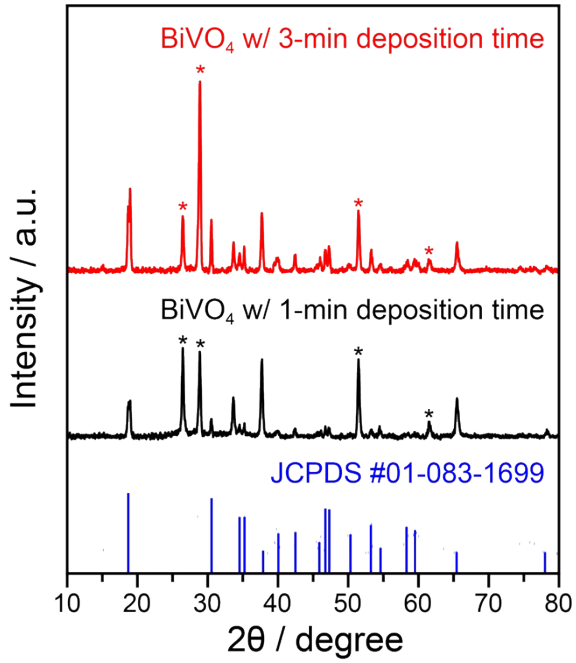

Fig. S5 X-ray diffraction (XRD) patterns of $BiVO_4$ with 1- and 3-min deposition time. For comparison, the standard diffraction pattern of JCPDS #01-083-1699 is given. Asterisks denote the XRD peaks of FTO.

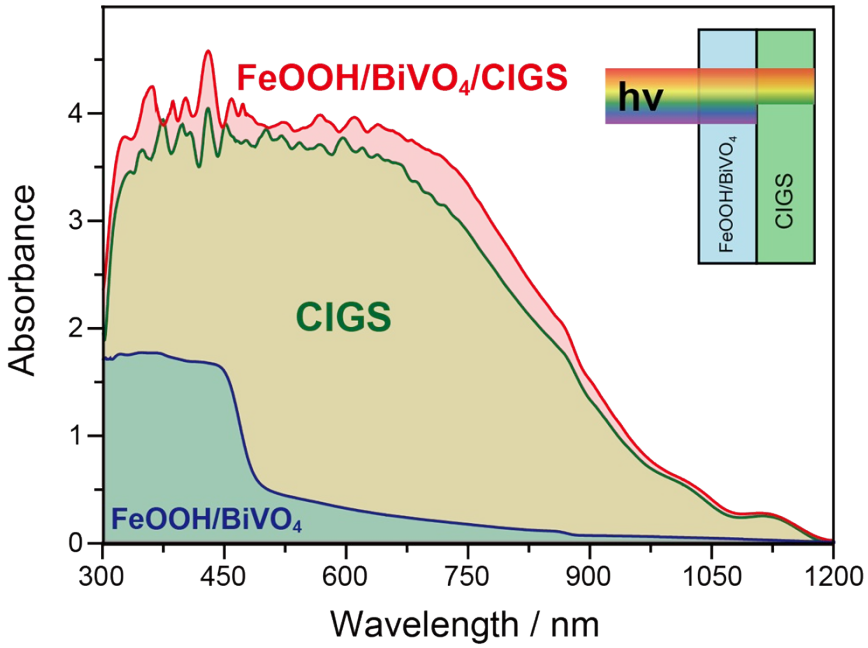

Fig. S6 Absorption spectra of $FeOOH/BiVO_4$, CIGS, and $FeOOH/BiVO_4$/CIGS. Note that we changed the substrate of the CIGS from an opaque Mo-coated soda-lime glass to a transparent soda-lime glass; the transmitted light through the CIGS film cannot penerate through the Mo layer and thus a spectrophotometer cannot analyze the absorption property of the CIGS film.

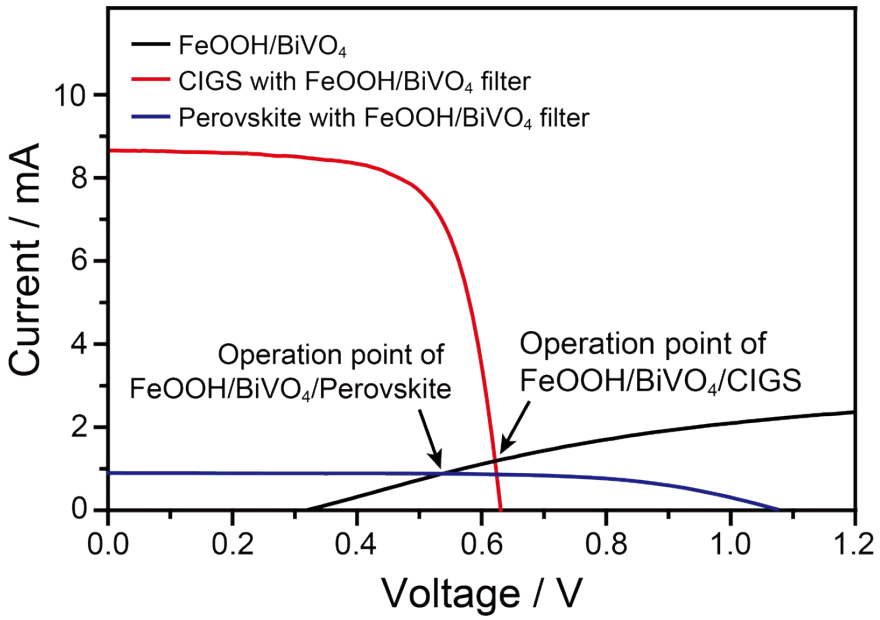

Fig. S7 Overlap of *I-V* profiles of $FeOOH/BiVO_4$, CIGS photovoltaic, and PSC. The y-value of the intersection indicates an estimated photocurrent of a tandem device (*i.e.*, $FeOOH/BiVO_4$/CIGS and $FeOOH/BiVO_4$/Perovskite). Geometrical surface areas of $FeOOH/BiVO_4$, CIGS, and perovskite: 4, 0.45, and 0.45 cm^2, respectively.

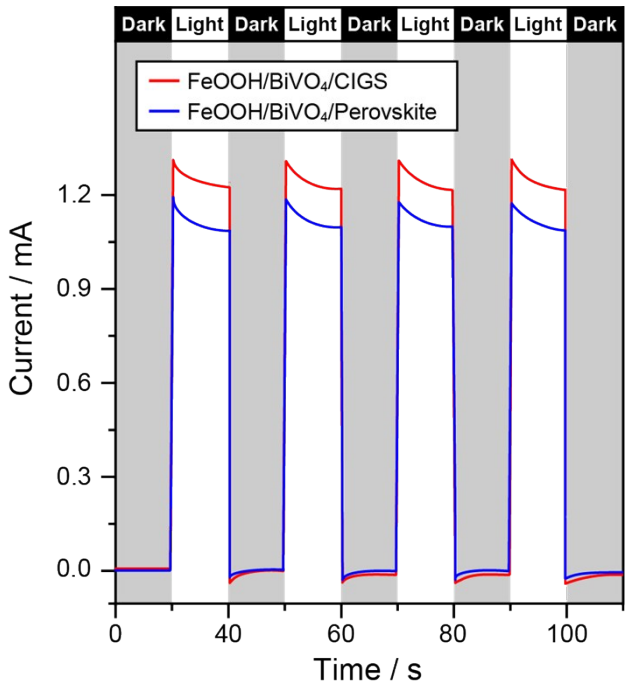

Fig. S8 Transient photocurrent responses of two different tandem devices in a two-electrode configuration at 0 V. Counter electrode: stainless steel. Electrolyte solution: sodium phosphate buffer (100 mM, pH 7.0).

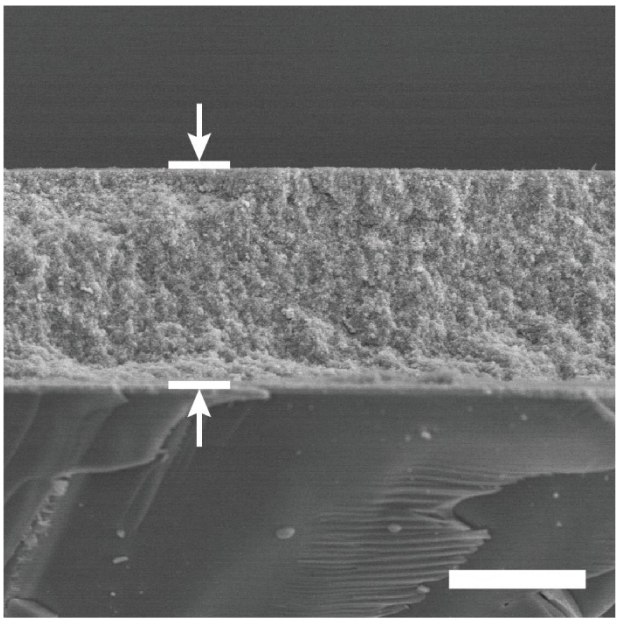

Fig. S9 Cross-sectional SEM image of *meso*ITO. Scale bar: 10 μm.

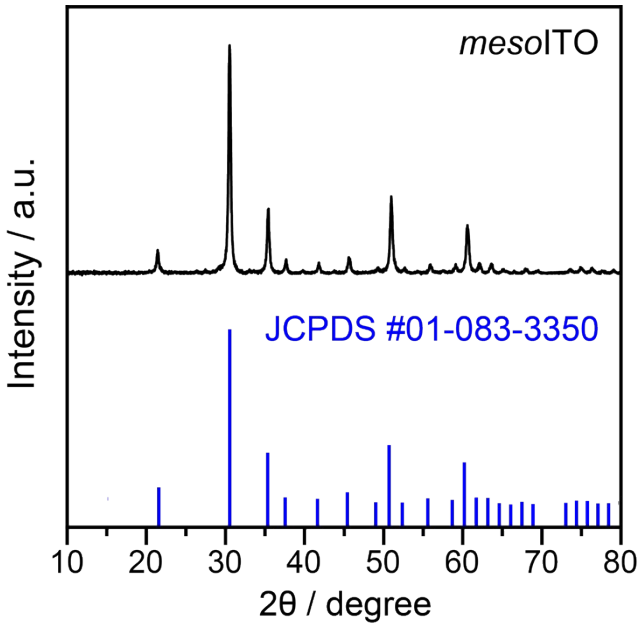

Fig. S10 XRD pattern of *meso*ITO. Below is the corresponding XRD peaks of ITO standard card (JCPDS #01-083-3350).

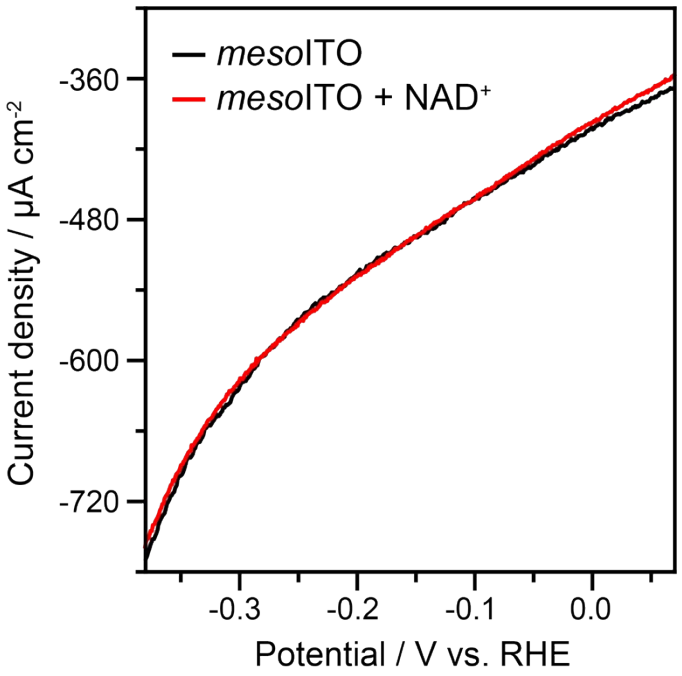

Fig. S11 Linear sweep voltammograms of *meso*ITO electrode (geometrical surface area: 1 cm^2) in the absence and presence of NAD^+. Scan rate: 20 mV s^{-1}. Counter electrode: stainless steel. Solvent: sodium phosphate buffer (100 mM, pH 7.0).

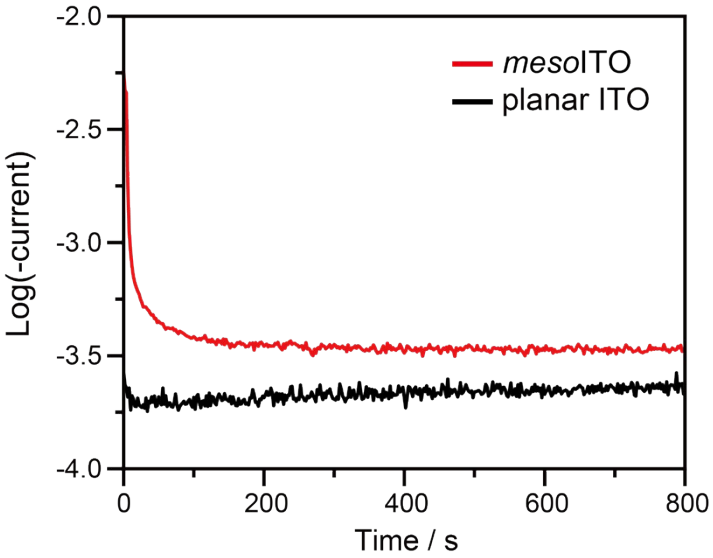

Fig. S12 Chronoamperograms of *meso*ITO and planar ITO electrodes for **M** reduction. Geometrical surface area: 1 cm^2. Applied bias: -0.28 V vs. RHE. Note that the unit of the antilogarithm of y-axis is the ampere. Counter electrode: stainless steel. Reaction conditions: 0.25 mM **M** in a sodium phosphate buffer (100 mM, pH 7.0) with stirring.

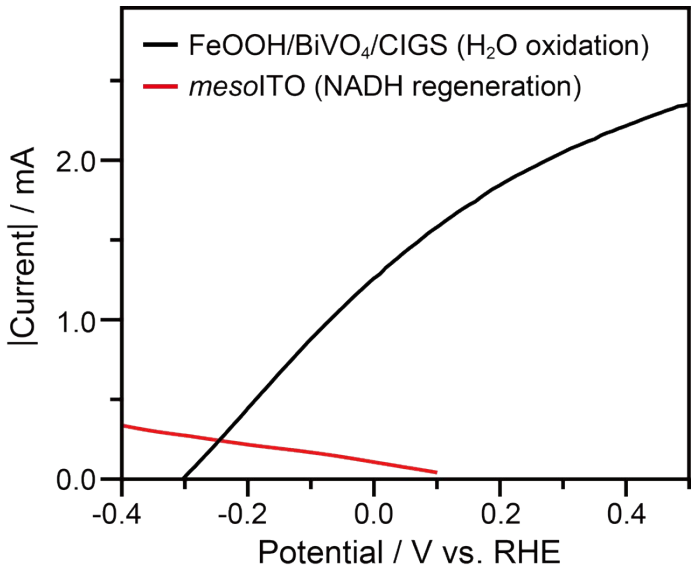

Fig. S13 Overlap of $|I|$-V plots of FeOOH/$BiVO_4$/CIGS device and *meso*ITO electrode for H_2O oxidation and NADH regeneration, respectively. Note that the $|I|$-V curve of the *meso*ITO was obtained as follows: we obtained (i) a $|I|$-V curve of *meso*ITO without **M** and NAD^+ and (ii) that with 0.5 mM **M** and 1 mM NAD^+ under stirring. Then, we subtracted the former curve from the latter curve to obtain the faradaic current by **M** reduction reaction in the presence of NAD^+. Geometrical surface areas of FeOOH/$BiVO_4$, CIGS, and *meso*ITO: 4, 0.45, and 1 cm^2, respectively. Light source: xenon lamp ($\lambda > 400$ nm, P: 100 mW cm^{-2}).

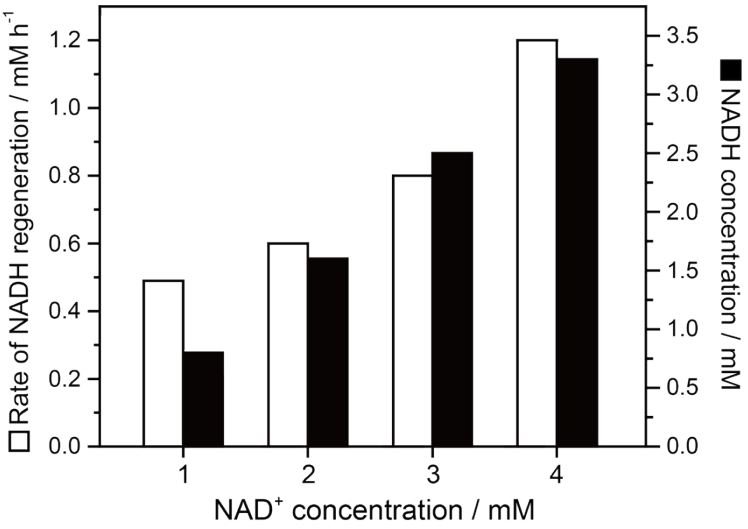

Fig. S14 Effect of NAD^+ concentration on NADH regeneration rate and NADH concentration. The regeneration rates were determined at 1-h reaction. Reaction condition: 0.5 mM **M** and NAD^+ dissolved in a sodium phosphate buffer (100 mM, pH 7.0, 2.5 ml). Working electrode: FeOOH/$BiVO_4$/CIGS. Counter electrode: *meso*ITO. Applied bias: 0 V. Light source: xenon lamp (P: 100 mW cm^{-2}, $\lambda > 400$ nm).

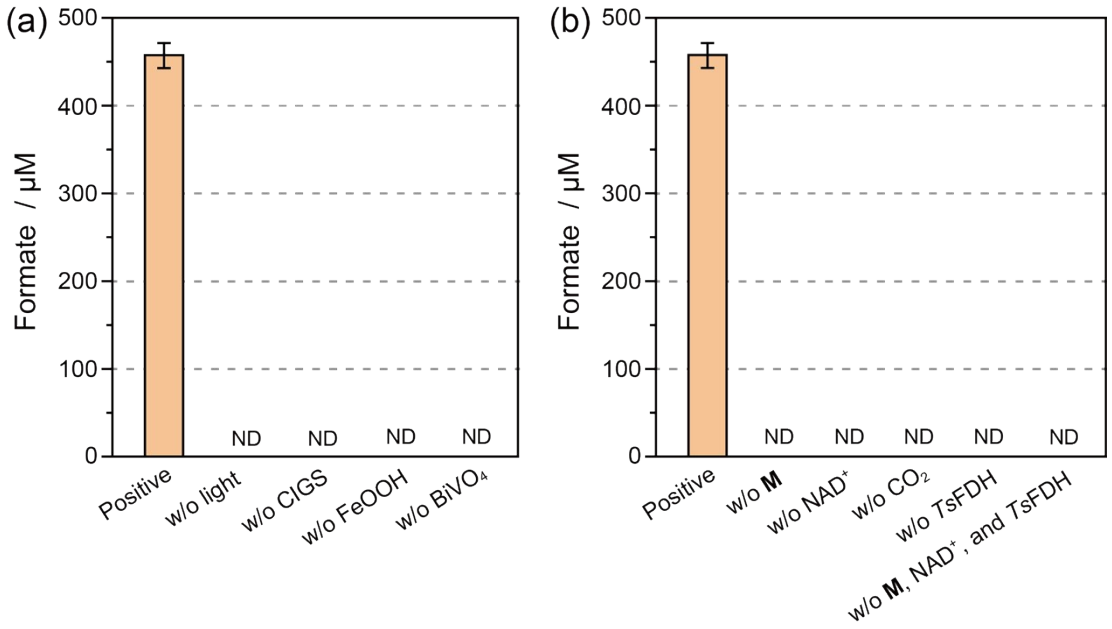

Fig. S15 Control experiments for unbiased photobiocatalytic CO_2-to-formate conversion in the absence of (**a**) light, CIGS, FeOOH, or $BiVO_4$ and (**b**) **M**, NAD^+, CO_2, or *Ts*FDH. Reaction condition of the experimental group: 0.5 mM **M**, 0.5 mM NAD^+, and 10 U ml^{-1} *Ts*FDH in a CO_2-purged phosphate buffer (100 mM, pH 7.0, 2.5 ml). Working electrode: FeOOH/$BiVO_4$/CIGS. Counter electrode: *meso*ITO. Light source: xenon lamp (*P*: 100 mW cm^{-2}, λ > 400 nm). Applied bias: 0 V. Reaction time: 4 h. ND: not detected.

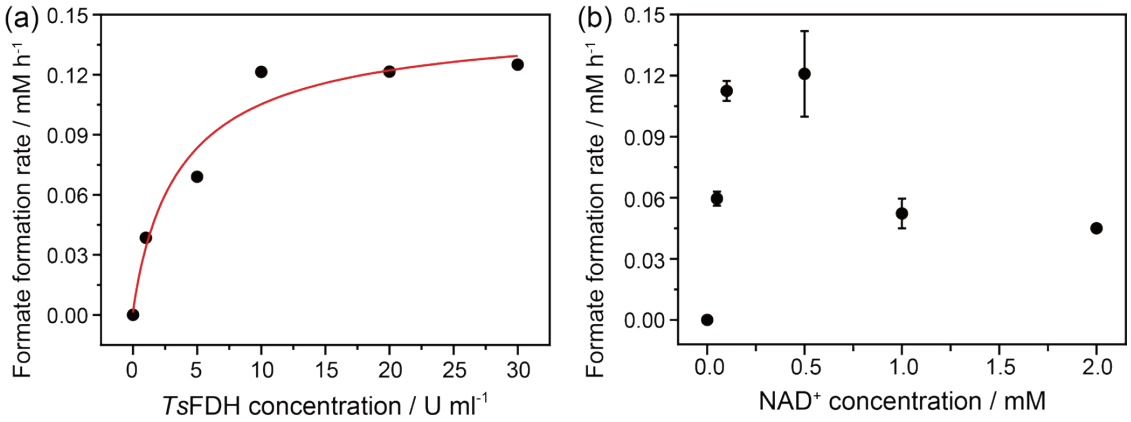

Fig. S16 Dependency of the rate of formate production on (**a**) *Ts*FDH concentration and (**b**) NAD^+ concentration. Reaction conditions of (**a**): 0.5 mM **M**, 0.5 mM NAD^+, and *Ts*FDH in a sodium phosphate buffer (100 mM, pH 7.0, 2 ml). Reaction condition of (**b**): 0.5 mM **M,** NAD^+, and 10 U ml^{-1} *Ts*FDH in a sodium phosphate buffer (100 mM, pH 7.0, 2.5 ml). Gaseous CO_2 (99.999%) was continuously purged before and during the experiment. Working electrode: FeOOH/$BiVO_4$/CIGS. Counter electrode: *meso*ITO. Applied bias: 0 V. Light source: xenon lamp (λ > 400 nm, *P*: 100 mW cm^{-2}).

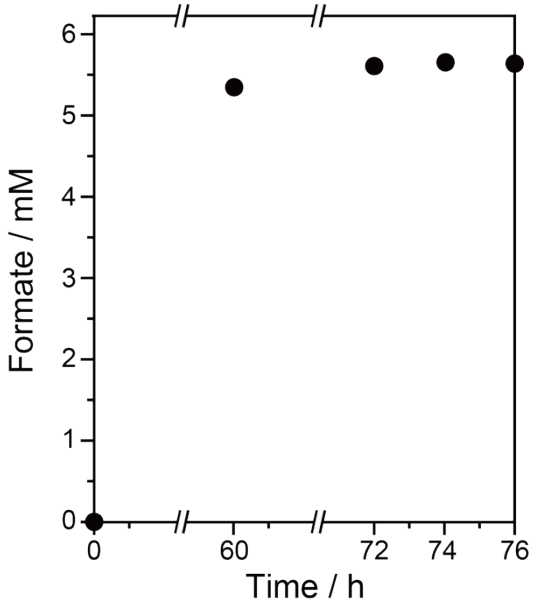

Fig. S17 Long-term biocatalytic conversion of CO_2 to formate using CIGS-based full tandem system. Reaction condition: 0.5 mM **M**, 0.5 mM NAD^+, and 10 U ml^{-1} *Ts*FDH in a sodium phosphate buffer (100 mM, pH 7.0, 2.5 ml). Working electrode: FeOOH/$BiVO_4$/CIGS. Counter electrode: *meso*ITO. Light source: xenon lamp (λ > 400 nm, *P*: 100 mW cm^{-2}). External bias: 0 V.

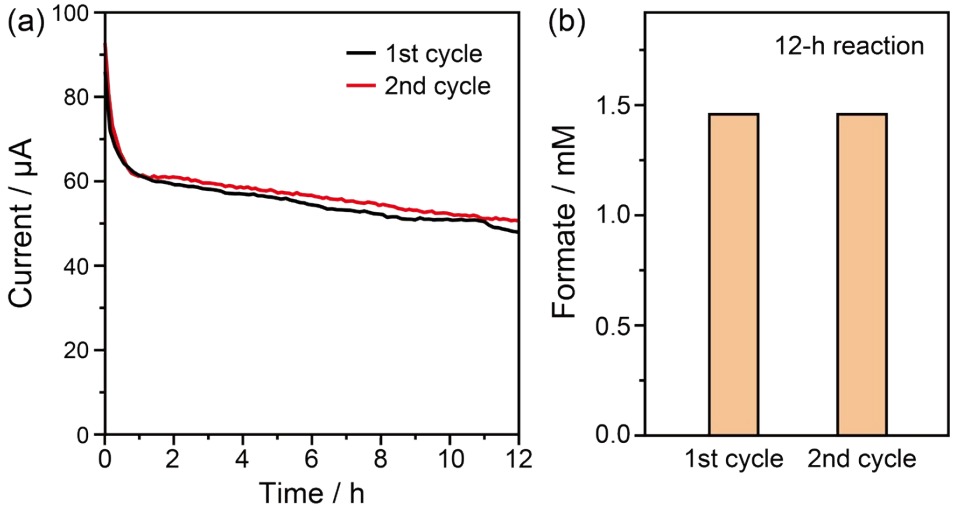

Fig. S18 (**a**) Bias-free controlled potential photoelectrolysis (CPPE) of CIGS-based full tandem device in the first and second cycle. (**b**) Formate concentration at 12-h biocatalytic PEC reaction of the first and second cycles. After the first cycle (72 h), we replaced the reaction solution and conducted the second CPPE. Reaction condition: 0.5 mM **M**, 0.5 mM NAD^+, and 10 U ml^{-1} *Ts*FDH in a sodium phosphate buffer (100 mM, pH 7.0, 2.5 ml). Working electrode: FeOOH/$BiVO_4$/CIGS. Counter electrode: *meso*ITO. Light source: xenon lamp (λ > 400 nm, *P*: 100 mW cm^{-2}).

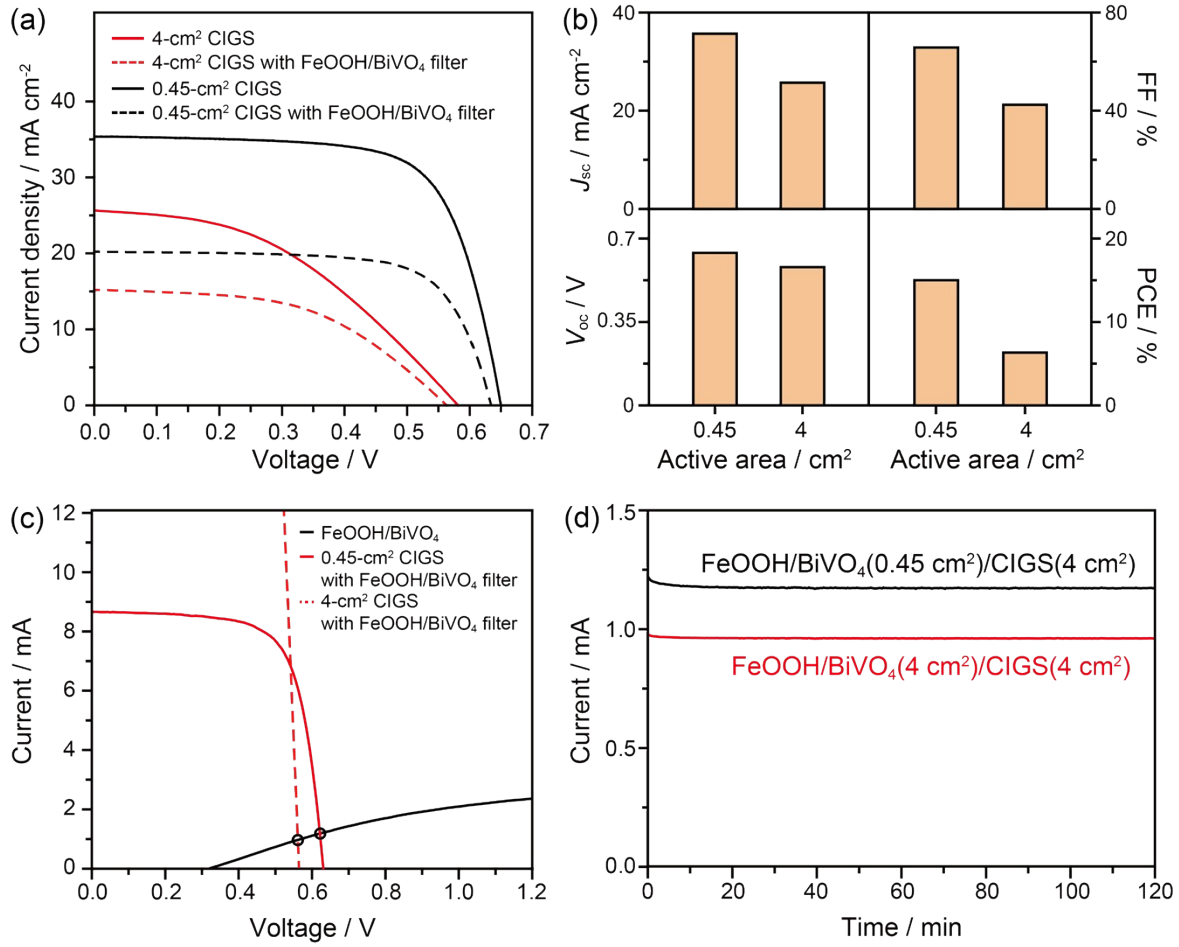

Fig. S19 (**a**) *J-V* curves of 0.45- and 4-cm^2 CIGS solar cells under illumination with/without FeOOH/$BiVO_4$-filtered light. (**b**) Photovoltaic parameters of 0.45- and 4-cm^2 CIGS solar cells. (**c**) Overlap of *I-V* profiles of FeOOH/$BiVO_4$, 0.45-cm^2 CIGS photovoltaic, and 4-cm^2 CIGS photovoltaic. Scan rate: 50 mV s^{-1}. The y-value of the intersection indicates an estimated photocurrent of a photoanode/photovoltaic tandem device. (**d**) Bias-free CPPE of FeOOH/$BiVO_4$/CIGS tandem devices in a two-electrode configuration. Counter electrode: stainless steel. Electrolyte solution of (**c**) and (**d**): sodium phosphate buffer (100 mM, pH 7.0). The upscaling of the CIGS's active area from 0.45 to 4 cm^2 decreased four photovoltaic parameters, such as J_{sc} (35.68 to 25.70 mA cm^{-2}), V_{oc} (0.64 to 0.58 V), FF (65 to 42 %), and PCE (15.01 to 6.32 %) (**Fig. S19(a) and S19(b)**). We attribute it to the compositional inhomogeneities in CIGS layer during CIGS deposition to large areas[12, 13], which is a well-known issue in the PV community. Under the FeOOH/$BiVO_4$-filtered light, the V_{oc} of the 4-cm^2 CIGS was lower than that of the 0.45-cm^2 CIGS (**Fig. S19(a)**). As a consequence, the estimated operation current of the FeOOH/$BiVO_4$/CIGS became lower by ca. 0.25 mA according to the intersection of the *J-V* curves of of the CIGS photovoltaic and the FeOOH/$BiVO_4$ photoanode (**Fig. S19(c)**). This is consistent with the decline in the actual photocurrent of the tandem device (**Fig. S19(d)**).

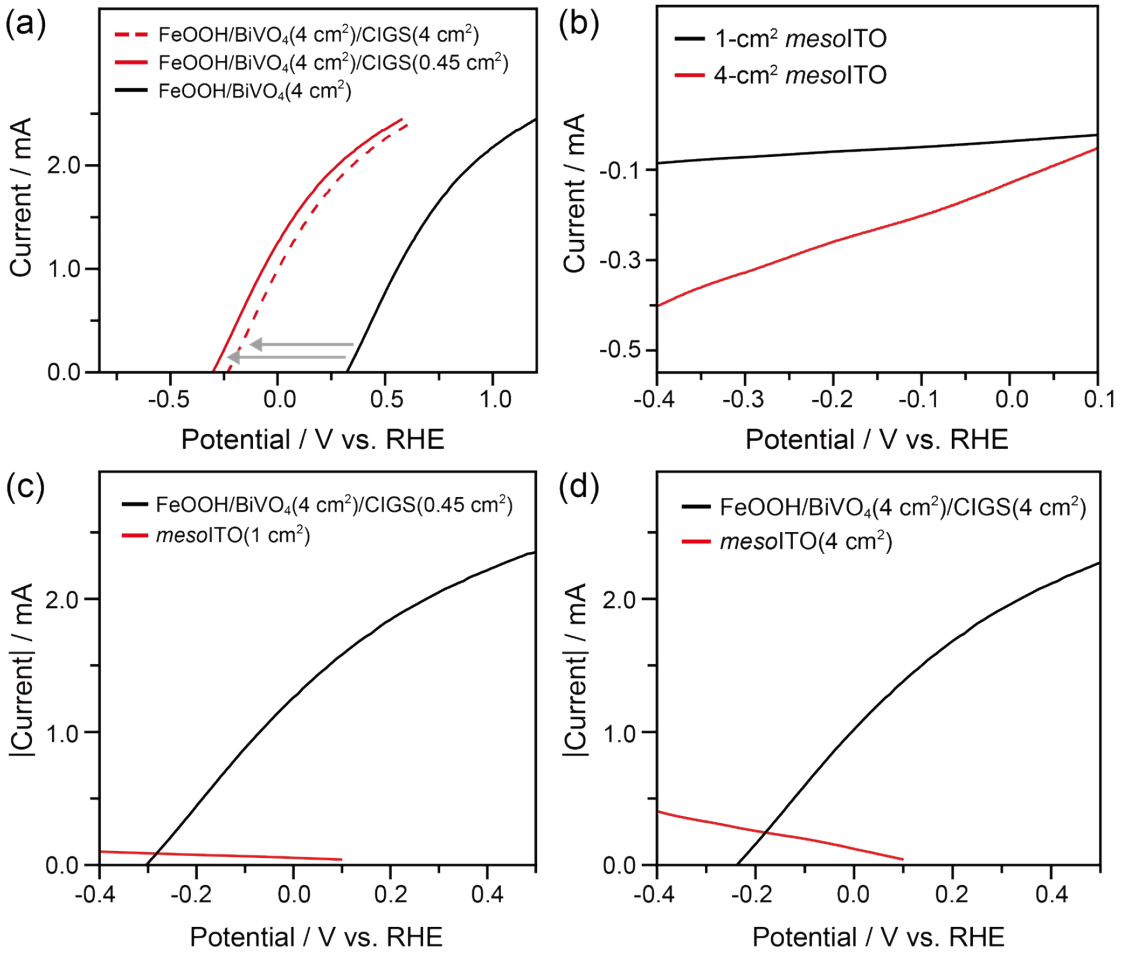

Fig. S20 (**a**) *I-V* curves of 4-cm^2 FeOOH/$BiVO_4$ and FeOOH/$BiVO_4$/CIGS with different active areas under light irradiation. (**b**) *I-V* curves of 1- and 4-cm^2 *meso*ITO electrodes for NADH regeneration. These plots were obtained as follows: we obtained (i) a |*I*|-*V* curve of *meso*ITO without **M** and NAD^+ and (ii) that with 0.5 mM **M** and 0.5 mM NAD^+ under stirring. Then, we subtracted the former curve from the latter curve to obtain the faradaic current by **M** reduction reaction in the presence of NAD^+. (**c, d**) Overlap of |*I*|-*V* plots of FeOOH/$BiVO_4$/CIGS device and *meso*ITO electrode with different active areas for unbiased coupling of H_2O oxidation with NADH regeneration. We assembled a 4-cm^2 full tandem device consisting of the FeOOH/$BiVO_4$/CIGS photoanode/photovoltaic and a *meso*ITO cathode. Although the 4-cm^2 CIGS shifted the *J-V* profile of the FeOOH/$BiVO_4$/CIGS less cathodically than the 0.45-cm^2 CIGS (**Fig. S20(a)**), the magnitude of the cathodic current of the *meso*ITO (for NADH regeneration) increased upon quadrupling of the *meso*ITO's geometrical surface area (**Fig. S20(b)**). As a result, the estimated operation current became higher for unbiased coupling of NADH regeneration with H_2O oxidation (**Fig. S20(c) and S20(d)**).

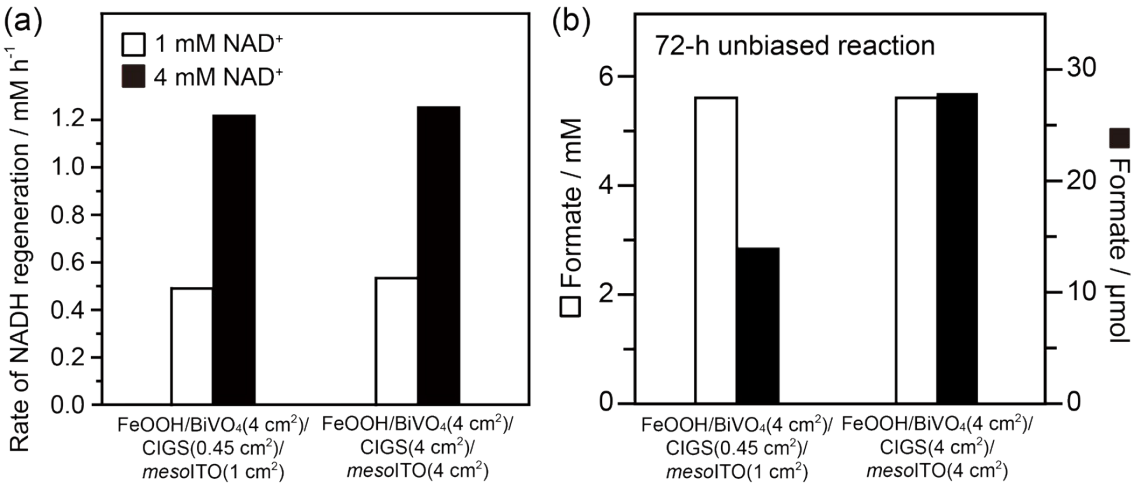

Fig. S21 (**a**) Influence of NAD^+ concentration on unbiased NADH regeneration rate at 1-h reaction. Reaction condition: 0.5 mM **M** and NAD^+ dissolved in a sodium phosphate buffer (100 mM, pH 7.0). (**b**) Concentrations and amounts of formate for 72-h biocatalytic photoelectrochemical reactions. Reaction condition: 0.5 mM **M**, 0.5 mM NAD^+, and 10 U ml^{-1} *Ts*FDH in a sodium phosphate buffer (100 mM, pH 7.0). Gaseous CO_2 (99.999%) was continuously purged before and during the experiment. Note that we increased an electrolyte volume in the cathodic compartment from 2.5 to 5.0 mL because we enlarged the *meso*ITO's surface area from 1 to 4 cm^2.

Supplementary references

1. J. Ryu, D. H. Nam, S. H. Lee and C. B. Park, *Chem. Eur. J.*, 2014, **20**, 12020-12025.
2. H. Choe, J. C. Joo, D. H. Cho, M. H. Kim, S. H. Lee, K. D. Jung and Y. H. Kim, *PLoS One*, 2014, **9**, e103111.
3. S. T. Kim, L. Larina, J. H. Yun, B. Shin and B. T. Ahn, *Sustain. Energ. Fuels*, 2019, **3**, 709-716.
4. P. Boonmongkolras, D. Kim, Esra M. Alhabshi, I. Gereige and B. Shin, *RSC Adv.*, 2018, **8**, 21551-21557.
5. J. Odrobina, J. Scholz, A. Pannwitz, L. Francàs, S. Dechert, A. Llobet, C. Jooss and F. Meyer, *ACS Catal.*, 2017, **7**, 2116-2125.
6. R. Chen, C. Yang, W. Cai, H.-Y. Wang, J. Miao, L. Zhang, S. Chen and B. Liu, *ACS Energy Lett.*, 2017, **2**, 1070-1075.
7. S. Cherevko, N. Kulyk and K. J. J. Mayrhofer, *Nano Energy*, 2016, **29**, 275-298.
8. J. Kim, S. H. Lee, F. Tieves, D. S. Choi, F. Hollmann, C. E. Paul and C. B. Park, *Angew. Chem. Int. Ed.*, 2018, **57**, 13825-13828.
9. D. H. Nam, S. K. Kuk, H. Choe, S. Lee, J. W. Ko, E. J. Son, E.-G. Choi, Y. H. Kim and C. B. Park, *Green Chem.*, 2016, **18**, 5989-5993.
10. E. J. Son, J. W. Ko, S. K. Kuk, H. Choe, S. Lee, J. H. Kim, D. H. Nam, G. M. Ryu, Y. H. Kim and C. B. Park, *Chem. Commun.*, 2016, **52**, 9723-9726.
11. H. Song, C. Ma, P. Liu, C. You, J. Lin and Z. Zhu, *J. CO_2 Util.*, 2019, **34**, 568-575.
12. V. Bermudez and A. Perez-Rodriguez, *Nat. Energy*, 2018, **3**, 466-475.
13. J. Ramanujam and U. P. Singh, *Energ. Environ. Sci.*, 2017, **10**, 1306-1319.